PACSIN2-dependent apical endocytosis regulates the morphology of epithelial microvilli

Meagan M. Postema[a], Nathan E. Grega-Larson[a], Leslie M. Meenderink[b], and Matthew J. Tyska[a,*]
[a]Department of Cell and Developmental Biology, Vanderbilt University School of Medicine, and [b]Division of Infectious Diseases, Department of Medicine, Vanderbilt University Medical Center, Nashville, TN 37232

ABSTRACT Apical microvilli are critical for the homeostasis of transporting epithelia, yet mechanisms that control the assembly and morphology of these protrusions remain poorly understood. Previous studies in intestinal epithelial cell lines suggested a role for the F-BAR domain protein PACSIN2 in normal microvillar assembly. Here we report the phenotype of PACSIN2 KO mice and provide evidence that through its role in promoting apical endocytosis, this molecule plays a role in controlling microvillar morphology. PACSIN2 KO enterocytes exhibit reduced numbers of microvilli and defects in the microvillar ultrastructure, with membranes lifting away from rootlets of core bundles. Dynamin2, a PACSIN2 binding partner, and other endocytic factors were also lost from their normal localization near microvillar rootlets. To determine whether loss of endocytic machinery could explain defects in microvillar morphology, we examined the impact of PACSIN2 KD and endocytosis inhibition on live intestinal epithelial cells. These assays revealed that when endocytic vesicle scission fails, tubules are pulled into the cytoplasm and this, in turn, leads to a membrane-lifting phenomenon reminiscent of that observed at PACSIN2 KO brush borders. These findings lead to a new model where inward forces generated by endocytic machinery on the plasma membrane control the membrane wrapping of cell surface protrusions.

INTRODUCTION

Apical specializations enable epithelial cells to carry out specific functions, including solute uptake and mechanosensation. In transporting epithelia, the apical surface is occupied by actin bundle–supported microvilli: finger-like protrusions that serve to amplify membrane surface area and maximize solute uptake capacity (Helander and Fandriks, 2014). A well-studied example is found in the intestinal tract where enterocytes, the most abundant epithelial cell type in the gut, provide the sole site of nutrient absorption. Enterocytes build tightly-packed arrays of thousands of microvilli, known as a brush borders. Microvillar growth and ordered packing take place as enterocytes differentiate, which occurs as they exit stem cell–containing crypt domains and move onto the villus surface (van Dongen et al., 1976; Specian and Neutra, 1981; Fath et al., 1990).

Microvillus formation requires coordination of a variety of activities, including actin filament nucleation, elongation, and bundling, which presumably all occur at the interface with the apical plasma membrane. Nucleation of the actin filaments that compose core bundles is at least partially controlled by the WH2-domain protein cordon bleu (COBL), which is required for normal brush border assembly in intestinal epithelial cell lines (Wayt and Bretscher, 2014; Grega-Larson et al., 2015, 2016). COBL overexpression drives microvillus elongation and also leads to protrusions that are straighter, with higher actin content (Grega-Larson et al., 2015). COBL localizes to microvillar rootlets, which are embedded in a dense subapical network of intermediate filaments known as the terminal web (Hirokawa et al., 1982). The actin-bundling protein fimbrin also localizes to the

terminal web and has been shown to link microvillar actin to keratin-19 in intermediate filaments (Grimm-Gunter et al., 2009). Along with fimbrin, two other bundling proteins, villin and espin, stabilize the core bundle in a region-specific manner (Bretscher and Weber, 1979, 1980; Mooseker et al., 1980; Bartles et al., 1998) and may promote elongation by slowing disassembly at the pointed ends (Loomis et al., 2003). Later in differentiation, epithelial-specific protocadherins target to the tips of microvilli to promote their elongation and tight packing (Crawley et al., 2014, 2016; Li et al., 2016, 2017; Weck et al., 2016; Yu et al., 2017). Such intermicrovillar adhesion allows cells to generate the maximum number of protrusions per unit apical surface area (Pinette et al., 2019).

Another recently identified factor that functions in microvillar growth is the I-BAR (inverse-Bin-Amphiphysin-Rvs) domain containing the insulin receptor tyrosine kinase substrate (IRTKS; Postema et al., 2018). BAR domains are small, three helix bundles that form curved dimers ~20 nm in length, which in turn form higher-order oligomers capable of sensing and inducing membrane curvature (Peter et al., 2004). I-BAR domains exhibit a structural curvature that is well matched to membrane bending away from the cell (Millard et al., 2005), like that found at the distal tips of microvilli. Indeed, IRTKS targets microvillar tips, where it promotes elongation directly by interacting with the core actin bundle, and indirectly through its interactions with epidermal growth factor receptor pathway substrate 8 (EPS8), another tip targeting factor implicated in the elongation of fingerlike protrusions (Croce et al., 2004; Disanza et al., 2006; Manor et al., 2011; Zampini et al., 2011; Postema et al., 2018).

In contrast to the curvature preference of I-BAR domains, F-BAR (Fes-CIP4 homology Bin-amphiphysin-Rvs161/167) motifs prefer binding to membranes that curve in toward the cytoplasm (Itoh et al., 2005; Frost et al., 2007; Henne et al., 2007). Protein kinase C and casein kinase substrate in neurons (PACSIN) family members are F-BAR proteins that have been implicated in a variety of cellular processes, including clathrin-dependent and -independent endocytosis, caveolae formation, vesicle trafficking, actin dynamics, and cell migration (Qualmann and Kelly, 2000; Qualmann et al., 2000; de Kreuk et al., 2011, 2012; Hansen et al., 2011; Senju et al., 2011; Chandrasekaran et al., 2016). Whereas PACSIN2 is widely expressed (Ritter et al., 1999), PACSIN1 exhibits specificity for neural tissues (Plomann et al., 1998), and PACSIN3 is expressed in heart and skeletal muscle (Sumoy et al., 2001). All three PACSIN isoforms contain an N-terminal F-BAR domain, along with a C-terminal SH3 domain. Interestingly, previous studies in intestinal epithelial cells revealed that PACSIN2 localizes to the intermicrovillar region in the terminal web, which exhibits a high degree of inward bending and also serves as the site of endocytosis (Grega-Larson et al., 2015). Moreover, through its SH3 domain, PACSIN2 also interacts with several binding partners with roles in actin filament nucleation and endocytosis at the membrane–cytoskeleton interface (Figure 1A). One example is the actin nucleator COBL, which interacts with PACSIN2 in the terminal web. Loss-of-function studies in intestinal epithelial cell lines suggest that PACSIN2 serves to recruit or anchor COBL at this location (Grega-Larson et al., 2015). COBL in turn uses its multiple WH2 domains to promote elongation of core actin bundles (Grega-Larson et al., 2016). In this context, PACSIN2 is critical for normal microvillar growth, as knocking down the molecule in cell-culture models leads to defects in brush border assembly (Grega-Larson et al., 2015). A second SH3 binding partner that links PACSIN2 to actin assembly is N-WASP, a nucleation-promoting factor and adaptor protein that activates the ubiquitous branched actin nucleator ARP2/3 (Padrick and Rosen, 2010). N-WASP interactions with PACSIN2 are believed to physically link the actin cytoskeleton

to membranes in processes such as endocytosis (Kessels and Qualmann, 2002, 2006). Yet another link between PACSIN2 and endocytosis is mediated by the SH3 domain binding to the large GTPase Dynamin2, which drives vesicle excision from the plasma membrane. PACSIN2 binds to and recruits Dynamin2 in the context of clathrin-mediated endocytosis and the internalization of caveolae (Kessels et al., 2006). Other studies have shown that the F-BAR domain of PACSIN2 is capable of oligomerizing and coating the necks of newly forming vesicles, which likely helps stabilize these intermediates before excision (Senju and Suetsugu, 2015).

In the present study, we sought to develop our understanding of PACSIN2 function in the epithelial apical domain through analysis of mice lacking PACSIN2 expression. Ultrastructural studies of tissues from knockout (KO) animals revealed a plasma membrane–lifting phenotype, where core actin bundles are no longer fully enveloped in membrane, and in some cases fuse with adjacent protrusions. Moreover, Dynamin2 and other endocytic factors were lost from their normal localization near the intermicrovillar endocytic region. To determine whether the loss of endocytic machinery could explain defects in brush border morphology, we examined the impact of dynamin inhibition and PACSIN2 KD on live intestinal epithelial cells. We found that when endocytic vesicle scission failed, tubules were pulled into the cytoplasm, and this led directly to a membrane-lifting phenomenon similar to that observed at PACSIN2 KO brush borders. Our findings illuminate a previously unrecognized link between endocytic function and the morphology of the epithelial apical domain and also suggest that inward forces generated on the plasma membrane by endocytic machinery control the membrane wrapping of cell surface protrusions.

RESULTS

PACSIN2 KO disrupts COBL localization

To explore how PACSIN2 contributes to enterocyte apical architecture and brush border assembly in vivo, we acquired mice expressing a PACSIN2[tm1b(EUCOMM)Hmgu] allele from the KOMP resource (Friedel et al., 2007). Tm1b mice are "CREed knockout first" and provide constitutive loss of expression in all tissues. KO of PACSIN2 was confirmed using Western blot analysis (Figure 1B). PACSIN2 KO mice did not exhibit gross-level phenotypes or defects in growth. Analysis of hematoxylin- and eosin-stained Swiss roll sections (Figure 1, C and D) and scanning electron microscopy (SEM) of duodenal tissue sections (Figure 1, E and F) revealed that PACSIN2 KO tissues were morphologically similar to those in the wild type (WT). In frozen sections of WT tissue, PACSIN2 is strongly enriched at the base of the brush border in the terminal web (Figure 1G). However, this labeling is completely lost in KO mice, further confirming loss of expression (Figure 1H). As previous studies in intestinal epithelial cells lines suggest that this F-BAR protein functions in the recruitment of COBL, we next sought to determine whether COBL was mislocalized in the absence of PACSIN2. As expected, COBL exhibits high-level enrichment in the terminal web of WT tissues (Figure 1I), but this labeling is significantly perturbed in KO samples (Figure 1J). This point was also confirmed by quantification of brush border–to–cytosol intensity ratios, which were markedly reduced in KO samples (2.83 ± 0.26 WT vs. 1.52 ± 0.18 KO; Figure 1K). Interestingly, in KO tissues, the COBL signal also appears redistributed along the microvillar axis (dashed arrows, Figure 1J), suggesting a role for PACSIN2 in anchoring COBL near microvillar rootlets. These results confirm the loss of PACSIN2 in the KO intestinal tissue and are consistent with previous studies indicating that PACSIN2 is needed for efficient targeting of COBL to the apical domain.
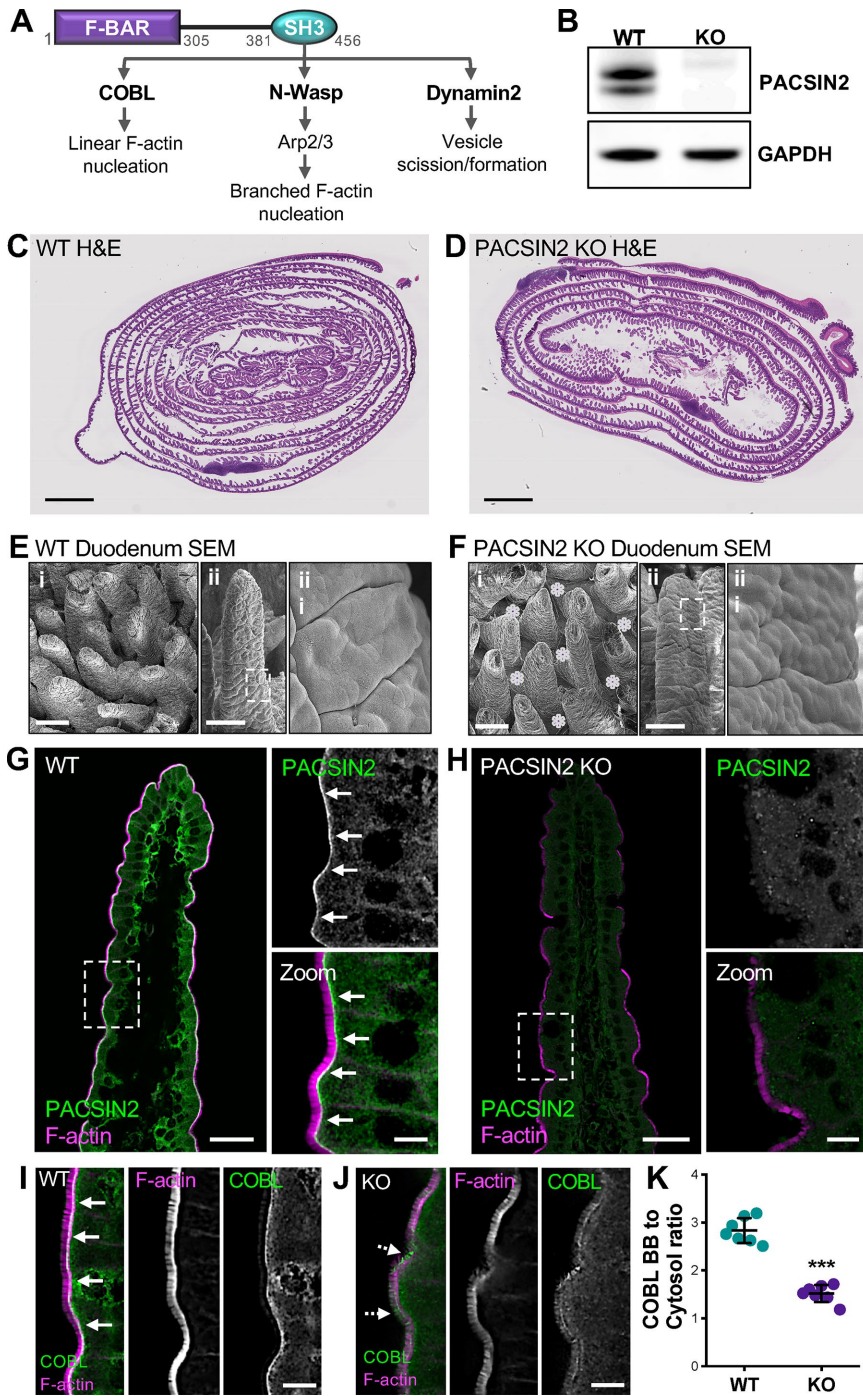
FIGURE 1: PACSIN2 KO disrupts COBL localization. (A) PACSIN2 domain diagram depicting SH3 binding partners and prospective functions. (B) Western blot of WT and PACSIN2 KO tissue with GAPDH as a loading control. (C, D) H&E-stained Swiss roll sections of paraffin-embedded small intestine from WT and PACSIN2 KO mice. Scale bars, 2 mm. (E, F) Scanning EM images of intestinal tissue samples from WT (E) and PACSIN2 KO (F) mice. Scale bars, 100 µm for i, 100 µm for ii, and 10 µm for iii; purple asterisks in KO *Bi* indicate bare spaces in the epithelium between adjacent villi. (G, H) Endogenous PACSIN2 (green) and phalloidin (F-actin, magenta) labeling of WT and PACSIN2 KO frozen tissue sections. Arrows highlight PACSIN2 signal at the base of the brush border in WT tissue, G. Scale bars, 50 µm for main panels, 10 µm for zooms.
(I, J) Endogenous COBL (green) and phalloidin (magenta) labeling of WT and PACSIN2 KO frozen tissue sections. Solid arrows highlight COBL signal at the base of the brush border in WT tissue (I); dashed arrows highlight mislocalization of COBL signal in KO tissue (J). Scale bars, 10 µm. (K) Quantification of the ratio of COBL brush border (BB) to cytosol signal intensity between the WT and PACSIN2 KO tissue; $n = 7$ tissue sections per condition. Error bars indicate ± SD; p value was calculated using a t test (***$p < 0.001$).

Loss of PACSIN2 decreases apical and basolateral F-actin levels

Given that PACSIN2 and its binding partners have been implicated in actin network assembly (Qualmann *et al.*, 2000; Kessels and Qualmann, 2004), we next sought to determine whether KO tissues exhibited perturbations in the actin cytoskeleton. Indeed, our initial staining of KO frozen tissue sections (Figure 1H) suggested that apical F-actin levels (assessed with phalloidin staining) were reduced, especially in the distal regions of villi. To examine this in greater detail, we performed volumetric imaging of whole mounted segments of intestinal tissue stained for F-actin. Three-dimensional reconstructions of individual villi revealed several striking defects in KO samples (Figure 2, A and B). Levels of F-actin appeared reduced throughout the apical domain, both in the brush border and at the lateral margins of cells (Figure 2, A and B). We also noted that the apical surfaces of individual cells exhibited a domed appearance, curving outward toward the lumen (Figure 2B). This phenotype was even more evident when we examined the apical surfaces of KO tissues using SEM (Figure 1, E and F). In higher-resolution tilted three-dimensional projections, KO brush borders demonstrated an apparent thinning of the F-actin signal, with certain regions exhibiting significantly reduced microvillar density relative to WT controls (Figure 2, C and E). Line scans drawn through the single-plane images (Figure 2, C and E, bottom panels) showed an almost twofold decrease in the PACSIN2 KO F-actin signal with several gaps throughout (maximum F-actin peak signal of 4095 for WT vs. 2156 for KO; Figure 2, D and F). Further quantification using thresholding and segmentation on multiple tissue sections also indicated a marked decrease in brush-border F-actin intensity in PACSIN2 KO tissues (mean intensity units 1912 ± 323 for WT vs. 1123 ± 239 for KO; Figure 2, G–I). Together, these data indicate that in the absence of PACSIN2, actin polymerization at the apical surface is compromised.

Given the striking reduction of apical F-actin signal observed at PACSIN2 KO brush borders, we also examined F-actin levels in actin networks in other parts of the cell (Figure 2, G and H). Mean F-actin intensity values, measured using a threshold that included all cellular structures basolateral to the brush border, were also markedly reduced (127.2 ± 34.5 WT vs. 82.7 ± 10.0 KO; Figure 2J). Interestingly, ratios of brush border/cell body F-actin intensities were unchanged in KO relative to WT samples (Figure 2K), suggesting that the overall
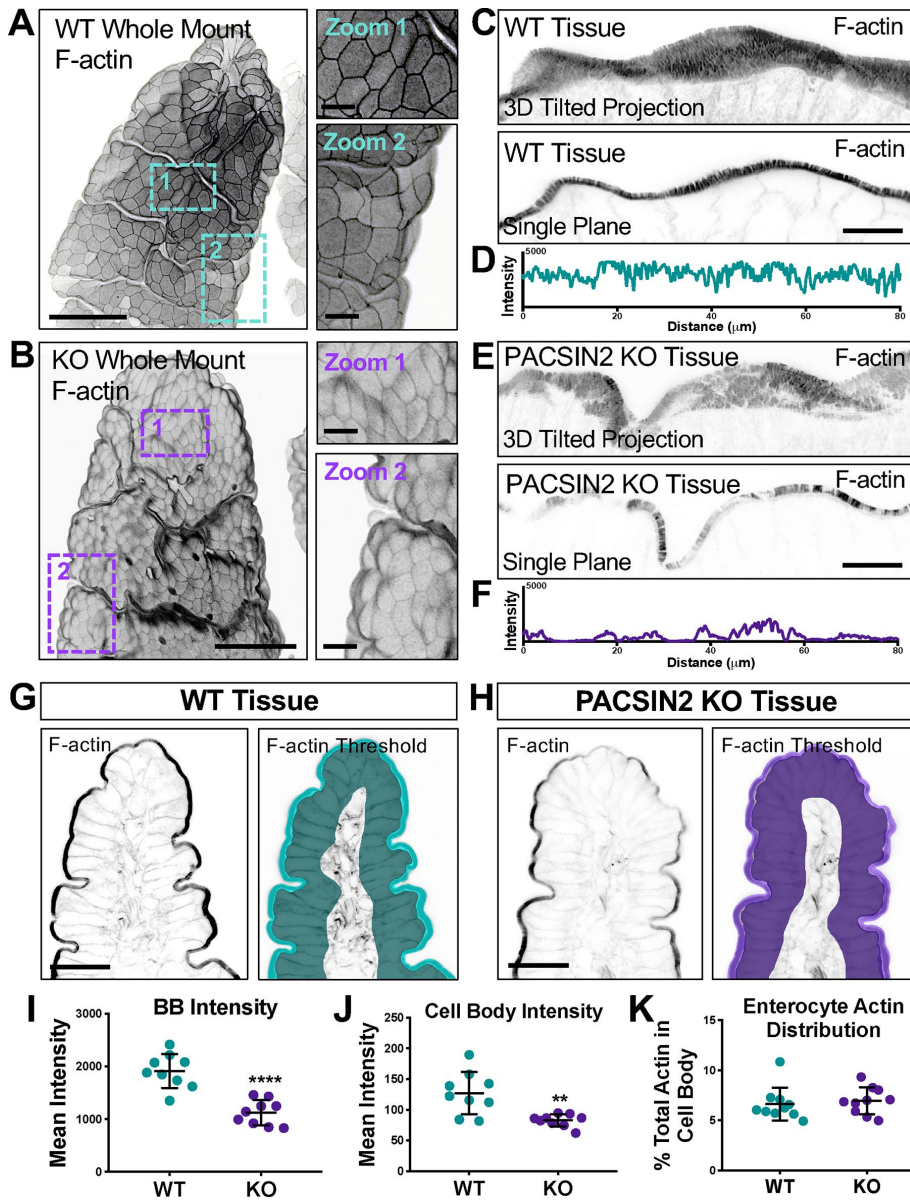
FIGURE 2: Loss of PACSIN2 decreases apical and basolateral F-actin levels. (A, B) Three-dimensional projections of 50-μm sections of WT (A) and PACSIN2 KO (B) whole mount tissue. Zooms highlight differences in cell surface morphology and actin intensity between WT and KO. Actin signal is inverted to simplify visualization; scale bars, 50 μm for main panels, 10 μm for zooms. (C, E) Three-dimensional reconstructed volumes of 8-μm sections, top, and single image planes, bottom, of phalloidin-stained WT and PASCIN2 KO frozen tissue sections. Scale bars, 25 μm. (D, F) Plots of raw 8-bit intensity data from an 80-μm line drawn through the brush border of the single plane images. PACSIN2 KO tissue has ~twofold decrease in brush border actin intensity. (G, H) Phalloidin labeling of WT and PACSIN2 KO frozen tissue sections. Right panels show representative thresholding of brush border and cell body used in quantification (I–K). Scale bars, 50 μm. (I) Quantification of brush border (BB) actin intensity between WT and PACSIN2 KO tissue; nine tissue sections per condition. (J) Quantification of cell body actin intensity between the WT and PACSIN2 KO tissue; nine tissue sections per condition. (K) Quantification of actin in the cell body as a percentage of total actin between WT and PACSIN2 KO; nine tissue sections per condition. Error bars indicate ± SD; p values were calculated using a t test (**$p < 0.01$, ****$p < 0.0001$).

at these sites (Supplemental Figure S1, G and J). Consistent with this, we also noted defects in the localization of tight and adherens junction markers ZO-1 and E-cadherin; both probes exhibited significantly lower levels of junctional enrichment than WT tissue sections (Supplemental Figure S1, K–M). These data indicate that in addition to promoting the growth of microvilli on the apical surface, PACSIN2 also drives the accumulation of F-actin at cell margins, where it promotes accumulation of factors that contribute to cell–cell adhesion.

Endocytic machinery is mislocalized in the absence of PACSIN2

In addition to scaffolding factors such as COBL and N-WASP, which promote actin polymerization in the apical and basolateral compartments, PACSIN2 has been implicated in endocytic function in epithelial cells. Therefore, we sought to determine whether the subapical endocytic compartment in the terminal web was disrupted in the absence of PACSIN2. Under normal conditions, Dynamin2 is highly enriched at the base of microvilli in the terminal web, the site of endocytic vesicle formation and fission (Figure 3A). However, upon KO of PACSIN2, this striking band of enrichment is lost (Figure 3B), which is also reflected in a significant decrease of the brush border–to–cytosol ratio for this signal (2.04 ± 0.76 WT vs. 1.20 ± 0.25 KO; Figure 3C). We also stained sections for VAMP4 (vesicle-associated membrane protein 4), which has established roles in endo- and exocytosis (Steegmaier et al., 1999; Nicholson-Fish et al., 2015). Similarly to Dynamin2, VAMP4 exhibits striking enrichment at the base of the brush border in WT samples (Figure 3D), but marked loss from this region in KO tissues (Figure 3E); brush border–to–cytosol ratios confirmed the redistribution of VAMP4 in the absence of PACSIN2 (1.86 ± 0.52 WT vs. 1.31 ± 0.45 KO; Figure 3F). Thus, in addition to disruption of F-actin assembly throughout the enterocyte, these results show that loss of PACSIN2 disrupts the normal enrichment of endocytic machinery, including Dynamin2 and VAMP4, in the subapical terminal web.

Loss of PACSIN2 disrupts microvillar ultrastructure and organization

To understand how loss of PACSIN2 impacts brush border architecture, we employed transmission electron microscopy (TEM) to visualize WT and PACSIN2 KO tissues at the ultrastructural level (Figure 4, A and B). TEM imaging of sections parallel to the microvillar axis allowed us to perform detailed morphometry. Strikingly, microvilli at PACSIN2 KO brush borders were significantly shorter than in the WT (1.93 ± 0.35 μm WT vs. 1.08 ± 0.31 μm KO; Figure 4C). We

distribution of actin polymer was similar. Further analysis of the cell-body F-actin signal revealed that most of the intensity is derived from the basolateral margins, at sites of cell–cell contact (Supplemental Figure S1, E–J). Line-scan analysis through multiple cells revealed that junctional F-actin levels were also significantly reduced
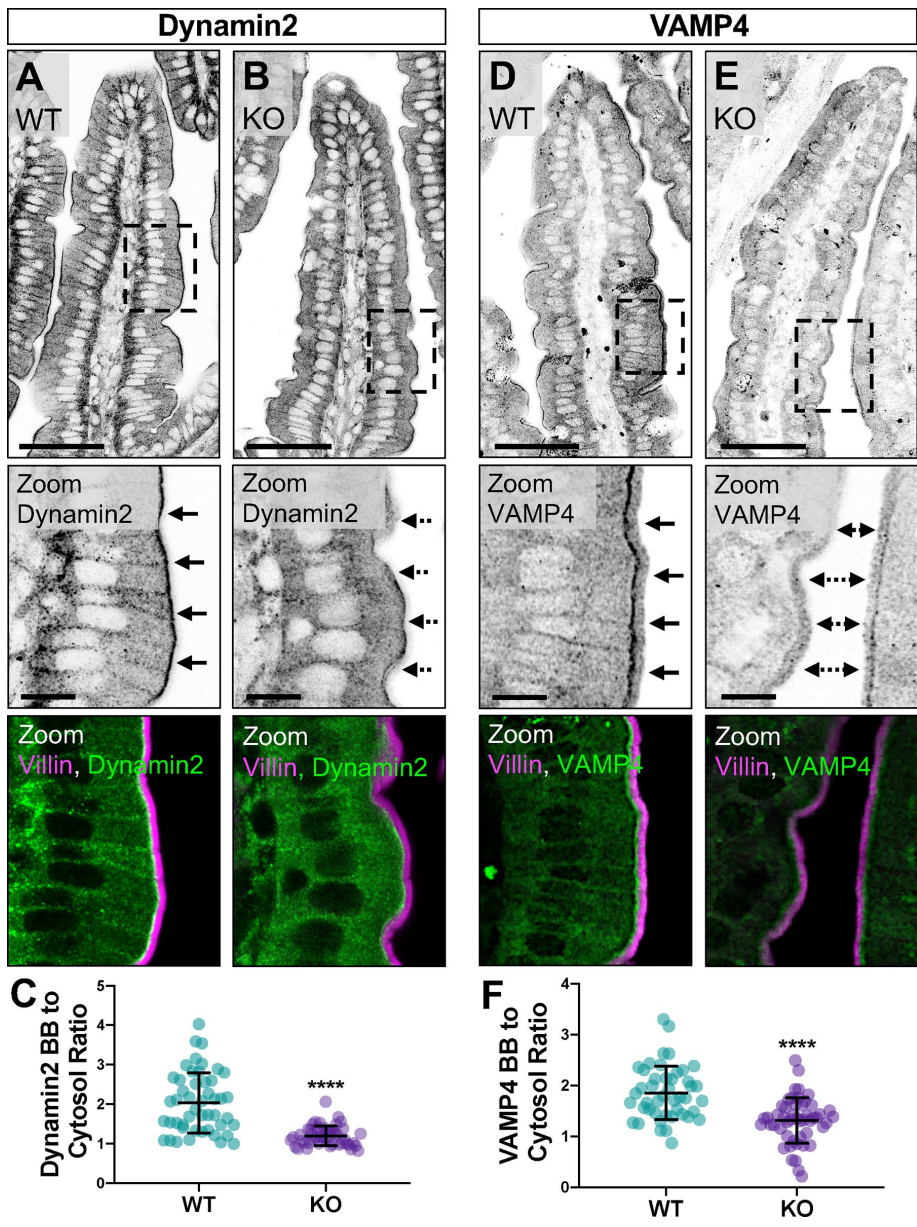
FIGURE 3: Endocytic machinery is mislocalized in the absence of PACSIN2. (A, B) Single confocal image planes of WT and PACSIN2 KO paraffin-embedded tissue sections stained with anti-Villin (magenta) to highlight the brush border and anti-Dynamin2 (green). Solid arrows in zoom panels highlight Dynamin2 signal at the base of the brush border in WT tissue (A); dashed arrows highlight mislocalization of Dynamin2 signal in KO tissue (B); scale bars, 50 µm for main panel, 10 µm for zoom. (C) Quantification of the ratio of Dynamin2 brush border (BB) to cytosol signal intensity between WT and PACSIN2 KO (n = 48 measurements). (D, E) Single confocal image planes of WT and PACSIN2 KO paraffin-embedded tissue sections stained with anti-Villin (magenta) and anti-VAMP4 (green). Solid arrows in zoom panels highlight VAMP4 signal at the base of the brush border in WT tissue (D); dashed arrows highlight mislocalization of VAMP4 signal in KO tissue (E); scale bars, 50 µm for main panel, 10 µm for zoom. (F) Quantification of the ratio of VAMP4 brush border (BB) to cytosol signal intensity between WT (n = 45 measurements) and PACSIN2 KO (n = 50 measurements). Error bars indicate ± SD; p values were calculated using a t test (****p < 0.0001).

$(0.47 \pm 0.12$ µm WT vs. 0.54 ± 0.15 µm KO; Figure 4E). In addition, we noted a much more irregular membrane profile in the intermicrovillar region (Figure 4, G and H). In KO enterocytes, the straightness of this profile was significantly reduced compared with WT controls $(0.87 \pm 0.08$ µm WT vs. 0.72 ± 0.11 µm KO; Figure 4I). Upon closer inspection of the PACSIN2 KO terminal web, we found an increased number of membrane invaginations extending into the cytoplasm, most likely stalled endocytic intermediates $(1.98 \pm 1.07$ WT vs. 4.25 ± 1.87 KO; Figure 4J). Combined with our staining data, these results indicate that loss of PACSIN2 disrupts endocytosis, which is associated with profound effects on microvillar morphology and the extent of membrane coverage.

To further analyze the organization of PACSIN2 KO brush borders, we performed SEM to visualize the apical surface. En face images immediately revealed perturbations in microvillar packing, with more apparent free space between adjacent protrusions (Supplemental Figure S2). We also examined intermicrovillar spacing by calculating nearest-neighbor distances (NNDs) for large numbers of protrusions. KO brush borders exhibited greater NND values with higher variability than in WT controls $(116.9 \pm 14.6$ nm WT vs. 131.8 ± 18.4 nm KO; Supplemental Figure S2C). To examine the impact of this increase in NND on the organization of microvilli, we calculated fast Fourier transforms (FFTs) as previously described (Pinette *et al.*, 2019). FFTs generated by WT brush borders exhibited the expected hexagonal pattern with six prominent first-order spots (Supplemental Figure S2D). However, FFTs generated from KO brush borders produced a pattern that lacked first-order spots, indicating a loss of ordered packing (Supplemental Figure S2E). These data reveal that microvilli at the PACSIN2 KO brush borders are less densely packed and no longer organized in the hexagonal arrays that are a defining feature of normal enterocyte brush borders.

Inhibition of endocytosis reduces microvillar membrane coverage

Our measurements indicate that under normal conditions, the distal ~80% of a microvillus actin core bundle is enveloped in apical plasma membrane (Figure 4F). In the absence of PACSIN2, membrane coverage

also found that the extent of membrane coverage, calculated as the percentage of the core actin bundle enveloped in the membrane, was significantly reduced at KO brush borders $(80.22 \pm 3.16\%$ WT vs. $66.34 \pm 7.10\%$ KO; Figure 4, B and F). Reduced membrane coverage was also linked to reduced actin core length $(2.41 \pm 0.44$ µm WT vs. 1.63 ± 0.39 µm KO; Figure 4D) and longer microvillar rootlets

is significantly reduced, with values that are much more variable across a population of protrusions (Figure 4F). By promoting endocytic activity and/or anchoring the intermicrovillar membrane to the actin cytoskeleton, PACSIN2 could play a direct role in controlling the extent of microvillar membrane coverage. Because mechanisms that control microvillar membrane coverage remain
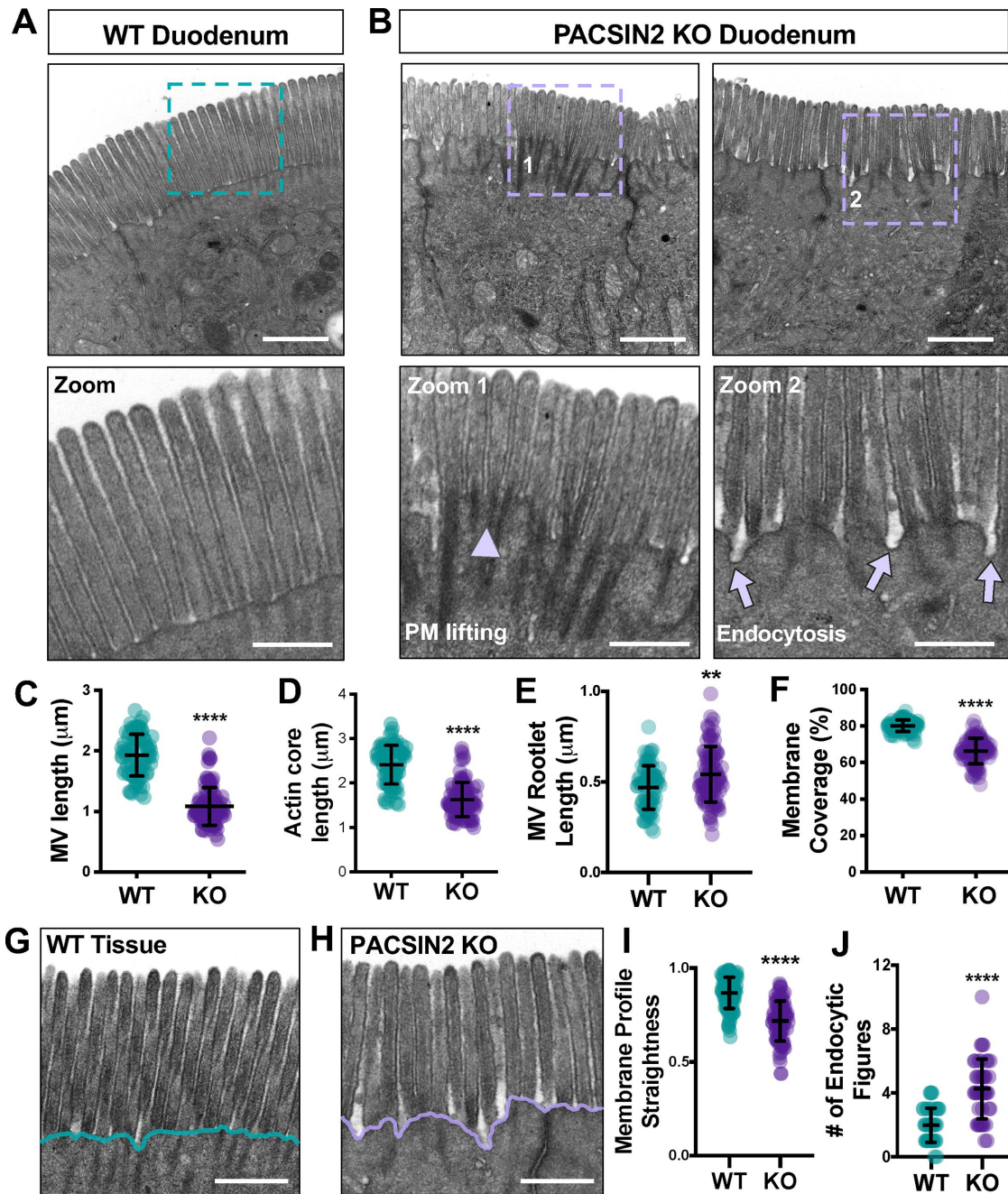
FIGURE 4: Loss of PACSIN2 disrupts microvillar ultrastructure and organization. (A) TEM image of a WT brush border in a plane parallel to the microvillar axis; teal dashed box indicates region highlighted in zoom panel below. Scale bar, 1 µm. (B) TEM images of PACSIN2 KO brush borders in a plane parallel to the microvillar axis; purple dashed boxes indicate region highlighted in zoom panels below. Arrowhead in zoom 1 highlights membrane lifting; arrows in zoom 2 highlight endocytic events. Scale bars, 1 µm. (C) Quantification of microvillar length (the length of an actin core covered in membrane) in WT ($n = 82$) and KO ($n = 102$). Measurements were selected so that only protrusions with actin cores fully visible along their length were scored. (D) Quantification of total microvillar actin core length in WT ($n = 83$) and KO ($n = 102$) microvilli. (E) Quantification of microvillar rootlet length in WT ($n = 83$) and KO ($n = 102$) microvilli. (F) Quantification of membrane coverage, the percentage of an actin core wrapped in membrane, in WT ($n = 83$) and KO ($n = 102$) microvilli. (G, H) Representative images of WT (F) and KO (G) tissue used in the quantification of membrane profile straightness (H); scale bars, 0.5 µm. Teal and purple lines highlight the decreased membrane straightness in KO. (I) Quantification of plasma membrane profile straightness at the base of WT ($n = 102$) and KO ($n = 88$) microvilli; total membrane length was measured over 1-µm units. (J) Quantification of the number of endocytic figures, or structures that resemble stalled endocytic intermediates, at the plasma membrane of WT ($n = 44$ image fields) and KO ($n = 44$ image fields) brush borders. Error bars indicate ± SD; p values were calculated using a t test (**$p < 0.01$, ****$p < 0.0001$).

poorly defined, we sought to test this hypothesis using the Ls174T-W4 (W4) intestinal epithelial cell culture model, which has been engineered to form microvilli upon exposure to doxycycline (Baas et al., 2004). Similarly to WT intestinal tissue, W4 cells demonstrate localization of PACSIN2 and Dynamin2 in the terminal web (Supplemental Figure S3, A and B).

We first sought to determine whether PACSIN2 KD in W4 cells generated a phenotype similar to what we observed with PACSIN2 KO mouse intestinal tissues. W4 cells transduced with scramble control shRNA or shRNA targeting PACSIN2 were fixed and stained to label the plasma membrane and underlying actin cytoskeleton and then imaged using superresolution structured illumination microscopy (SIM). KD of PACSIN2 significantly decreased microvillar membrane coverage relative to that in scramble controls (78.3 ± 8.6% KD vs. 89.1 ± 6.2% SCR) (Figure 5, A–C). We also imaged PACSIN2 KD W4 cells live using spinning disk confocal microscopy (SDCM). Remarkably, time-lapse acquisitions revealed the formation of long aberrant membrane tubules, presumably stalled endocytic intermediates, which originated in the intermicrovillar region (Figure 5E). Coincident with the formation of these tubules, we noted significant apical membrane lifting, which exposed the rootlets of adjacent microvillar core actin bundles, in a manner that was strikingly reminiscent of membrane coverage perturbations observed in PACSIN2 KO brush borders (Figure 4). Thus, in terms of the microvillar membrane coverage, PACSIN2 KD in W4 cells phenocopies the defects observed in brush borders from PACSIN2 KO mice.

We next set out to determine whether the microvillar membrane coverage defects observed in PACSIN2 KO tissues and KD W4 cells were due specifically to perturbations in endocytic activity. For these experiments, we exposed differentiating W4 cells to Dynasore, a small molecule inhibitor of the GTPase domain of Dynamin2 that is expected to prevent the scission of endocytic vesicles from the apical membrane. Dynasore-treated W4 cells were fixed and stained to visualize the actin cytoskeleton and plasma membrane, and then imaged using SIM. Remarkably, exposure to Dynasore decreased microvillar membrane coverage significantly relative to that in control DMSO-treated cells (77.2 ± 9.1% Dynasore vs. 89.0 ± 6.9% DMSO; Figure 5, F–H). We also used SDCM to image the impact of Dynasore treatment on live W4 cells. Similarly to that observed in PACSIN2 KD W4 cells, we noted the formation of long aberrant membrane tubules, which again originated in the intermicrovillar region (Figure 5J). The formation of these tubules also coincided with significant membrane lifting and exposure of microvillar core bundle rootlets (Figure 5J). We verified this effect using a second inhibitor of endocytosis, Pitstop 2, which generated similar aberrant tubule formation and membrane lifting (Figure S3D). Together, these findings uncover a previously unrecognized link between PACSIN2-dependent endocytic activity and the extent of microvillar membrane coverage. These data further suggest that inward forces on the apical membrane, normally generated by endocytic machinery, serve to control microvillar morphology.

DISCUSSION

PACSIN family proteins have long been implicated in the regulation of actin assembly in the context of membrane deformation during endocytosis and vesicle formation. Indeed, in the initial report, PACSIN1 (primarily expressed in neural tissues) coimmunoprecipitated with synaptic vesicle endocytic factors including dynamin, synaptojanin, and synapsin-1, as well as N-WASP, an actin nucleation–promoting factor that activates the ARP2/3 complex (Qualmann et al., 1999). All of these interactions were mediated through the PACSIN1 C-terminal SH3 domain (Qualmann et al., 1999). During endocyto-

sis, PACSINs are believed to recruit N-WASP, which in turn targets ARP2/3 to generate bursts of actin filament polymerization in the space between the plasma membrane and nascent budding vesicles. Combined with activity of Dynamin GTPase, which constricts the necks of forming vesicles, these bursts of actin polymerization likely generate additional mechanical force for efficient vesicle scission (Kessels and Qualmann, 2002, 2004). Although PACSINs have been implicated in various forms of endocytosis, including activity-dependent bulk endocytosis (ADBE) and clathrin-mediated endocytosis (Qualmann and Kelly, 2000), PACSIN2 has more recently been implicated in caveolar endocytosis, where it binds to the necks of nascent caveolae and recruits Dynamin2 to promote vesicle scission (Hansen et al., 2011; Senju et al., 2011; Senju and Suetsugu, 2015). In support of an endocytic role in transporting epithelia, previous studies localized PACSIN2 to the subapical terminal web region of native enterocytes in the mouse small intestine and human W4 cells in culture (Grega-Larson et al., 2015). In the terminal web, endocytic vesicles are formed from the inwardly curving membrane found between neighboring microvilli (Danielsen and Hansen, 2016). Indeed, SIM imaging of differentiated W4 cells revealed robust PACSIN2 localization in the intermicrovillar region, immediately between adjacent core actin bundles (Grega-Larson et al., 2015). In the present study, we found that markers of endocytosis that are normally enriched in the terminal web, including Dynamin2 and VAMP4, were also lost from this region in the absence of PACSIN2. Together, all of these data establish a role for PACSIN2 in the normal targeting of endocytic machinery to the subapical compartment.

In addition to a role in apical endocytic vesicle formation, PACSIN2 was found to play a role in recruiting the linear actin nucleator, COBL, to the terminal web. In the W4 cell culture model, COBL loss of function impairs brush border assembly, whereas overexpression promotes the formation of microvillar actin cores in a manner that depends on the number WH2 domains (Grega-Larson et al., 2015, 2016). COBL is also recruited to the apices of epithelial cells, coincident with the earliest events in brush border assembly (Grega-Larson et al., 2015). Consistent with its role in targeting COBL to the terminal web, we found significantly lower levels of COBL at the base of the brush border in PACSIN2 KO tissues. PACSIN2 KO enterocytes also exhibited reduced apical actin levels as assessed with the F-actin reporter phalloidin (Figure 2). Confocal volume projections showed a clear thinning of brush border F-actin signal, with reduced microvillar density and regions that appeared to lack microvilli completely (Figure 2, C and E). In the ultrastructural analysis of KO tissues, we also noted a significant decrease in microvillar length (Figure 4C). Together, these findings suggest that KO of PACSIN2 and subsequent loss of COBL from the terminal web impair the production of actin filaments that form microvillar actin core bundles.

Remarkably, measurements of phalloidin intensity from other parts of PACSIN2 KO enterocytes revealed lower levels of F-actin, although the apical/cell body F-actin signal ratio remained unchanged in response to PACSIN2 KO (Figure 2K). Because most of the cell body signal derives from the basolateral margins, we propose that these perturbations are induced by loss of N-WASP–stimulated ARP2/3 activity at the basolateral cortex. In support of this, previous studies showed that inactivation of ARP2, a component of the ARP2/3 complex, decreased actin polymerization and impairs the morphology and stability of epithelial adherens junctions (Yamazaki et al., 2007; Tang and Brieher, 2012). Inhibition of actin polymerization also impairs adherens junction reassembly and reduces E-cadherin enrichment (Ivanov et al., 2005a, 2005b; Kovacs et al., 2011). Interestingly, in our studies, the loss of junctional actin correlates with the loss of ZO-1 and E-cadherin signal in the
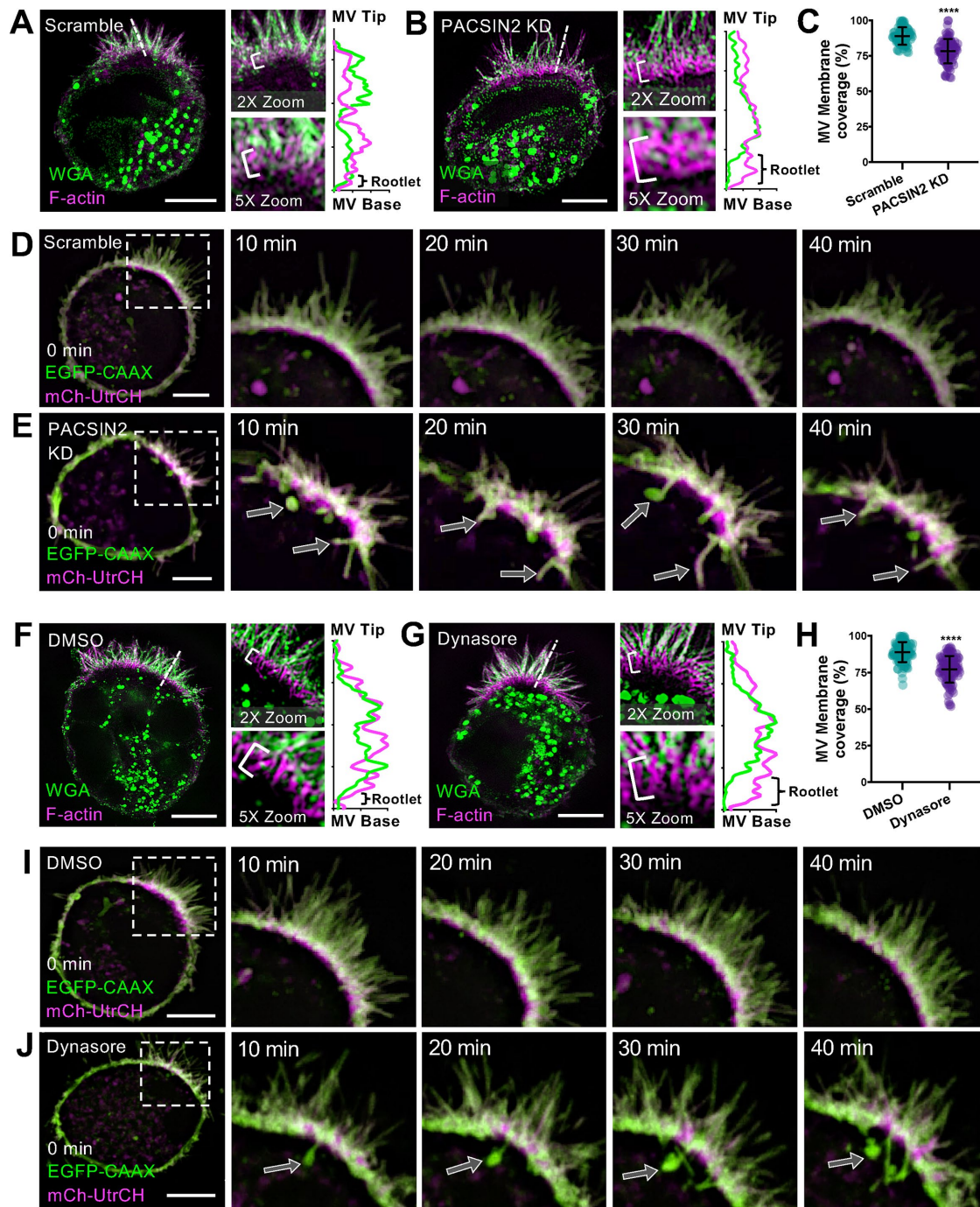
FIGURE 5: Inhibition of endocytosis reduces microvillar membrane coverage. (A, B) SIM projections of scramble control (A) and PACSIN2 KD (B) W4 cells stained for WGA (membrane, green) and phalloidin (magenta). Brackets in zoom panels indicate actin rootlet lengths. Dashed lines denote where line scans were drawn through a single microvillus to show increased actin rootlet length; membrane (green), actin (magenta). Scale bars, 5 µm. (C) Quantification of microvillar membrane coverage; scramble $n = 77$ microvilli from 10 cells; PACSIN2 KD $n = 88$ microvilli from 11 cells. (D, E) Montages of scramble control and PACSIN2 KD W4 cells expressing EGFP-CAAX box (last 10aa of the GTPase HRas; membrane, green) and mCherry-UtrCH (F-actin, magenta). Arrows in the PACSIN2 KD cell (E) indicate membrane tubules forming into the cytosol. Scale bars, 5 µm. (F, G) SIM projections of DMSO control– (F) and 80 µM Dynasore– (G) treated W4 cells stained for WGA (membrane, green) and phalloidin (magenta). Brackets in zoom panels indicate actin rootlet lengths. Dashed lines denote where line scans were drawn to show increased actin rootlet length: membrane (green), actin (magenta). Scale bars, 5 µm. (H) Quantification of microvillar membrane coverage; DMSO $n = 104$ microvilli from 13 cells; Dynasore $n = 105$ microvilli from 12 cells. (I, J) Montages of DMSO control– and 80 µM Dynasore–treated W4 cells expressing EGFP-CAAX box (membrane, green) and mCherry-UtrCH (F-actin, magenta). Arrows in the Dynasore-treated cell (J) indicate membrane tubules forming into the cytosol. Scale bars, 5 µm. Error bars indicate ± SD; p values were calculated using a t test (****$p < 0.0001$).

PACSIN2 KO mouse (Supplemental Figure S1), indicating a disruption in normal junctional stability and architecture.

Perhaps the most unexpected finding from the current investigation was the striking perturbation of microvillar ultrastructure in PACSIN2 KO brush borders. We observed a significant decrease in microvillar length and the extent of membrane coverage, that is, the fraction of core actin bundle encapsulated in plasma membrane. These changes were accompanied by a corresponding increase in the length of exposed rootlet. How does loss of PACSIN2 impact microvillar structure and membrane coverage? While it is known that membrane–cytoskeleton linkers, such as Myo1a and Ezrin, stabilize physical contact between the plasma membrane and the underlying actin core, factors that control the extent of membrane coverage are poorly understood. A clue to the mechanism might come from our observation of a higher frequency of membrane invaginations originating from the intermicrovillar region in PACSIN2 KO brush borders. Because PACSIN2 and its binding partners (e.g., Dynamin) normally stimulate vesicle scission at these sites, the elongated invaginations that extend through the terminal web are most likely stalled endocytic structures, an interpretation consistent with their tubular morphology. Indeed, PACSIN2 KD in cultured cells has been shown to generate elongated caveolae (Senju *et al.*, 2011). If the entire apical membrane is composed of a single continuous surface, the formation of exaggerated tubules in the terminal web will directly reduce the amount of membrane material available for encapsulating microvilli and thus compromise the extent of membrane coverage. To test this possibility more directly, we modeled the defects observed in PACSIN2 KO tissues in the W4 intestinal epithelial cell line. PACSIN2 KD in this context also leads to reduced membrane coverage of microvilli. Strikingly, we also observed that the inward pull of exaggerated tubules temporally coincides with loss of membrane coverage on microvilli immediately adjacent to these sites. Because we were able to phenocopy these events with two distinct inhibitors of endocytosis, we conclude that the exaggerated tubules observed in PACSIN2 KO and PACSIN2 KD cells are in fact stalled endocytic intermediates. Together, our findings highlight a mechanistic link between subapical endocytic activity and the membrane coverage of apical microvilli.

Interestingly, a role for inward-pulling forces on the apical plasma membrane in shaping fingerlike protrusions has been highlighted in previous studies of the pointed end–directed motor MYO6. MYO6 localizes to the terminal web, where it interacts with endocytic machinery near the pointed ends of microvillar core actin bundles, including DAB2, and GIPC (Tumbarello *et al.*, 2013). In Snell's Waltzer mice, which lack functional MYO6, inner ear hair cells exhibit a membrane-lifting phenotype similar what we observe at PACSIN2 KO brush borders (Self *et al.*, 1999). These cells also manifest with fused or coalesced protrusions, where multiple core bundles appear to be enveloped in a single tubule of plasma membrane. Later studies with the same model system revealed similar phenomena in the enterocyte brush border, with marked decreases in the membrane coverage of core actin bundles and more general disorder in the terminal web (Hegan *et al.*, 2012). In combination with the data we present here, these studies lead to a model where the formation and steady-state morphology of fingerlike protrusions such as microvilli and stereocilia are controlled by a balance of outward and inward mechanical forces that impinge on the plasma membrane. PACSIN2 likely limits these forces by promoting the budding and scission of endocytic vesicles from the intermicrovillar membrane. Whether PACSIN2 functions in the same pathway as MYO6 is not known, but functional links between these two factors should be the focus of future studies.

MATERIALS AND METHODS

Frozen tissue preparation
Segments of WT and KO intestine were removed, flushed with phosphate-buffered saline (PBS), and prefixed for 10 min with 4% paraformaldehyde (PFA) to preserve the tissue structure. The tube was then cut along its length, subdissected into 0.5 μm–square chunks, fixed for additional 30 min in 4% PFA at room temperature (RT), and washed three times in PBS. Samples were then gently placed on top of a 30% sucrose solution in TBS and allowed to sink to the bottom overnight at 4°C. Specimens were then swirled in three separate blocks of OCT (Electron Microscopy Sciences), oriented in a block filled with fresh OCT, and snap frozen in dry ice-cooled acetone. Samples were cut into 10-μm sections and mounted on slides for staining.

Cell culture
Ls174T-W4 cells (female *Hs* colon epithelial cells) were cultured in DMEM with high glucose and 2 mM L-glutamine supplemented with 10% tetracycline-free fetal bovine serum (FBS), G418 (1 mg/ml), blasticidin (10 μg/ml), and phleomycin (20 μg/ml). The cell line was obtained from Hans Clevers (Utrecht University, the Netherlands) and has not been additionally authenticated. All cells were grown at 37°C under 5% CO_2.

Transfections and lentivirus production
All transfections were performed using Lipofectamine 2000 (Invitrogen) according to the manufacturer's instructions, and the cells were allowed to recover overnight (ON). Lentivirus was generated by cotransfecting HEK293FT cells (Fetal *Hs* embryonic epithelial cells; T75 flasks at 80% confluency) with 6 μg of pLKO.1 PACSIN2 shRNA KD plasmids (Open Biosystems; TRCN0000037980), 4 μg of psPAX2 packaging plasmid, and 0.2 μg of pMD2.G envelope plasmid using FuGENE 6 (Promega). Cells were incubated up to 48 h, and then lentivirus-containing medium was collected and concentrated with Lenti-X concentrator (Clontech). To transduce W4 cells in T25 flasks, lentiviral shRNAs with 6 μg/ml polybrene (Sigma) was added to the medium dropwise. After a 24-h incubation, the medium was changed and resupplemented with lentiviral shRNAs for an additional 24 h. The cells were then seeded into six-well plates with glass coverslips, incubated ON in the absence or presence of 1 μg/ml doxycycline, and then prepared for immunofluorescence.

Immunofluorescence
Frozen tissue sections of WT and PACSIN2 KO intestinal tissue were washed three times in PBS and permeabilized for 10 min with 0.1% Triton X-100/PBS at RT. The tissue sections were then blocked with 10% bovine serum albumin (BSA) at 37°C for 2 h and washed once with PBS. Primary antibodies (listed below) were diluted in 10% BSA/PBS and incubated with cells at 4°C ON, followed by four washes with PBS. Tissue sections were then stained with phalloidin and secondary antibodies (listed below) in 1% BSA/PBS for 2 h at RT, washed three times with PBS, and mounted with Prolong Gold Antifade mounting medium (P36930; Invitrogen). Paraffin-embedded small intestinal tissue sections of WT and PACSIN2 KO were deparaffinized using Histo-clear solution (Fisher) and rehydrated in a descending graded-ethanol series. Slides were then subject to an antigen retrieval step consisting of boiling for 1 h in a solution of 10 mM Tris (pH 9.0) and 0.5 mM ethylene glycol-bis(β-aminoethyl ether)-*N,N,N′,N′*-tetraacetic acid (EGTA). Slides were then washed three times in PBS and stained ON at 4°C with primary antibodies (see below) in 10% BSA/PBS. After being washed four times with PBS, samples were stained with secondary antibodies in 1% BSA/PBS for

2 h at RT. Slides were then washed four times with PBS and mounted in ProLong Gold Antifade mounting media.

For SIM imaging, cells were plated on glass coverslips and allowed to adhere for at least 6 h. They were then washed with prewarmed PBS and fixed for 15 min with 4% PFA/PBS at 37°C. Cells were then washed three times with PBS and permeabilized for 15 min with 0.1% Triton X-100/PBS at RT. Cells were once again washed three times with PBS and blocked for 1 h at 37°C in 5% BSA/PBS. Primary antibodies (listed below) were diluted in 1% BSA/PBS and incubated for 1 h with cells at 37°C, followed by four washes with PBS. Cells were then incubated for 1 h with secondary antibodies and phalloidin (listed below) at RT. Coverslips were then washed four times with PBS and mounted on glass slides in ProLong Gold Antifade Mounting Media. For live-cell spinning-disk confocal imaging of W4 cells, previously transfected cells were plated on glass-bottom dishes with 1 µg/ml doxycycline and allowed to adhere for 6 h. If drug treatments were performed, 80 µM DMSO/80 µM Dynasore (D7693; Sigma-Aldrich) or 30 µM DMSO/30 µM Pitstop 2 (SML1169; Sigma-Aldrich) was diluted into 1 ml medium and added to a glass-bottom dish of W4s 10 min before acquisition. For live imaging of scramble/PACSIN2 KD cells, the protocol above was used; however, cells were seeded into glass-bottom dishes instead of six-well plates, induced with 1 µg/ml doxycycline, and allowed to adhere for at least 4–6 h before imaging. Movies of single W4 cells were acquired every 5 s for 30 min or continuously for 4 min. All live cells were maintained in a humid environment at 37°C under 5% CO_2 using a stage-top incubation system. Image acquisition was controlled with Nikon Elements software.

The following dilutions were used for primary antibodies for staining: anti-PACSIN2 (2.5 µg/ml, HPA049854; Sigma-Aldrich), anti-COBL (1 µg/ml, HPA019033; Sigma-Aldrich), anti-Dynamin2 (4 µg/ml, NBP2-47477; Novus Biologicals), anti-villin (4 µg/ml; Santa Cruz #sc-66022), anti–E-cadherin (0.5 µg/ml; BD Biosciences #610182), anti-ZO-1 (5 µg/ml, 61-7300; Thermo Fisher), anti-VAMP4 (2 µg/ml, HPA050418; Sigma-Aldrich), and anti-RAB14 (4 µg/ml; Invitrogen #PA5-55306). The following dilutions were used for secondary antibodies and cell dyes for staining: goat anti-rabbit Alexa Fluor 488 F(ab')2 Fragment (2 µg/ml, A11070; Molecular Probes), goat anti-mouse Alexa Fluor 488 F(ab')2 Fragment (2 µg/ml, A11017; Molecular Probes), Alexa Fluor 568–phalloidin (1:200, A12380; Invitrogen), or Wheat Germ Agglutin Oregon Green (WGA; 2 µg/ml, W67-48; Life Technologies).

Light microscopy
Confocal microscopy was performed using a Nikon A1R laser-scanning confocal microscope equipped with 60×/1.4 NA and 100×/1.49 NA objectives. SIM was performed using a Nikon N-SIM with an Apo TIRF 100×/1.49 NA objective. All images used for quantitative comparisons were prepared with equal treatment, acquired with identical parameters (e.g. pinhole diameter, detector gain), and processed in an identical manner. Richardson–Lucy deconvolution of image volumes (20 iterations) was performed using Nikon Elements software. Live-cell imaging of W4 cells was performed on a Nikon Yokogawa CSU-X1 spinning-disk confocal microscope. Images were contrast-enhanced and cropped using ImageJ software (National Institutes of Health).

Electron microscopy
Segments of WT and KO intestine were placed in 0.1M HEPES (pH 7.3) and subdissected into 2-mm chunks at RT. Samples were placed in scintillation vials, incubated in RT fix buffer (4% PFA, 2.5% glutar-aldehyde, 2 mM $CaCl_2$ in 0.1M HEPES) for 1 h, and washed three times in HEPES buffer. Samples were incubated with 1% tannic acid/HEPES for 1 h and washed three times with ddH_2O, followed by incubation with 1% osmium tetroxide/ddH_2O for 1 h. Samples were then washed three times with ddH_2O, incubated in 1% uranyl acetate/ddH_2O for 30 min, and then washed with ddH_2O. Samples were dehydrated in a graded ethanol series and then dried using critical point drying. Samples were then mounted on aluminum stubs and coated with gold/palladium using a sputter coater. Imaging was performed using a Quanta 250 Environmental SEM operated in high-vacuum mode with an accelerating voltage of 5 kV. All EM reagents were purchased from Electron Microscopy Sciences.

Image analysis and statistics
All image analysis and signal intensity measurements from image data were performed using FIJI or Nikon Elements software. To perform intensity analyses (Figures 1, 2, and 6), the brush border and/or cytosol were thresholded in confocal villar images using Nikon Elements software and the mean intensity numbers per villus were plotted; brush border–to–cytosol enrichment was defined as the ratio of these two mean intensities. Microvillar length measurements were performed on projected SIM images (Supplemental Figure S3) or on TEM images (Figure 4) by tracing individual microvillar actin bundles using FIJI. For W4 cell microvillar length analysis, at least 10 microvillar actin bundles were scored per cell and at least 25 cells were measured per experiment. Microvillar membrane coverage measurements were performed on projected W4 SIM images (Figure 5) or on TEM images by dividing the length of a microvillus covered in membrane by the length of the entire actin bundle from the rootlet to the tip. Nearest-neighbor distance measurements (Figure 3) were performed by thresholding microvilli in SEM images using Nikon Elements. Data were analyzed with a D'Agostino and Pearson omnibus normality test to determine normal distribution and normally distributed data were statistically analyzed to determine significance using the unpaired Student's t test. Welch's correction was used in cases where data sets did not exhibit equal variance. Statistical analyses performed are stated in the figure legends. All graphs were generated and statistical analyses performed using Prism (v.7, GraphPad).

Animal studies
Animal experiments were carried out in accordance with Vanderbilt University Medical Center Institutional Animal Care and Use Committee guidelines.

REFERENCES
Baas AF, Kuipers J, van der Wel NN, Batlle E, Koerten HK, Peters PJ, Clevers HC (2004). Complete polarization of single intestinal epithelial cells upon activation of LKB1 by STRAD. Cell 116, 457–466.

Bartles JR, Zheng L, Li A, Wierda A, Chen B (1998). Small espin: a third actin-bundling protein and potential forked protein ortholog in brush border microvilli. J Cell Biol 143, 107–119.

Bretscher A, Weber K (1979). Villin: the major microfilament-associated protein of the intestinal microvillus. Proc Natl Acad Sci USA 76, 2321–2325.

Bretscher A, Weber K (1980). Fimbrin, a new microfilament-associated protein present in microvilli and other cell surface structures. J Cell Biol 86, 335–340.

Chandrasekaran R, Kenworthy AK, Lacy DB (2016). Clostridium difficile Toxin A undergoes clathrin-independent, PACSIN2-dependent endocytosis. PLoS Pathog 12, e1006070.

Crawley SW, Shifrin DA Jr, Grega-Larson NE, McConnell RE, Benesh AE, Mao S, Zheng Y, Zheng QY, Nam KT, Millis BA, et al. (2014). Intestinal brush border assembly driven by protocadherin-based intermicrovillar adhesion. Cell 157, 433–446.

Crawley SW, Weck ML, Grega-Larson NE, Shifrin DA Jr, Tyska MJ (2016). ANKS4B is essential for intermicrovillar adhesion complex formation. Dev Cell 36, 190–200.

Croce A, Cassata G, Disanza A, Gagliani MC, Tacchetti C, Malabarba MG, Carlier MF, Scita G, Baumeister R, Di Fiore PP (2004). A novel actin barbed-end-capping activity in EPS-8 regulates intestinal cells of Caenorhabditis elegans. Nat Cell Biol 6, 1173–1179.

Danielsen EM, Hansen GH (2016). Small molecule pinocytosis and clathrin-dependent endocytosis at the intestinal brush border: two separate pathways into the enterocyte. Biochim Biophys Acta 1858, 233–243.

de Kreuk BJ, Anthony EC, Geerts D, Hordijk PL (2012). The F-BAR protein PACSIN2 regulates epidermal growth factor receptor internalization. J Biol Chem 287, 43438–43453.

de Kreuk BJ, Nethe M, Fernandez-Borja M, Anthony EC, Hensbergen PJ, Deelder AM, Plomann M, Hordijk PL (2011). The F-BAR domain protein PACSIN2 associates with Rac1 and regulates cell spreading and migration. J Cell Sci 124(Pt 14), 2375–2388.

Disanza A, Mantoani S, Hertzog M, Gerboth S, Frittoli E, Steffen A, Berhoerster K, Kreienkamp HJ, Milanesi F, Di Fiore PP, et al. (2006). Regulation of cell shape by Cdc42 is mediated by the synergic actin-bundling activity of the Eps8-IRSp53 complex. Nat Cell Biol 8, 1337–1347.

Fath KR, Obenauf SD, Burgess DR (1990). Cytoskeletal protein and mRNA accumulation during brush border formation in adult chicken enterocytes. Development 109, 449–459.

Friedel RH, Seisenberger C, Kaloff C, Wurst W (2007). EUCOMM—the European conditional mouse mutagenesis program. Brief Funct Genomic Proteomic 6, 180–185.

Frost A, De Camilli P, Unger VM (2007). F-BAR proteins join the BAR family fold. Structure 15, 751–753.

Grega-Larson NE, Crawley SW, Erwin AL, Tyska MJ (2015). Cordon bleu promotes the assembly of brush border microvilli. Mol Biol Cell 26, 3803–3815.

Grega-Larson NE, Crawley SW, Tyska MJ (2016). Impact of cordon-bleu expression on actin cytoskeleton architecture and dynamics. Cytoskeleton (Hoboken) 73, 670–679.

Grimm-Gunter EM, Revenu C, Ramos S, Hurbain I, Smyth N, Ferrary E, Louvard D, Robine S, Rivero F (2009). Plastin 1 binds to keratin and is required for terminal web assembly in the intestinal epithelium. Mol Biol Cell 20, 2549–2562.

Hansen CG, Howard G, Nichols BJ (2011). Pacsin 2 is recruited to caveolae and functions in caveolar biogenesis. J Cell Sci 124(Pt 16), 2777–2785.

Hegan PS, Giral H, Levi M, Mooseker MS (2012). Myosin VI is required for maintenance of brush border structure, composition, and membrane trafficking functions in the intestinal epithelial cell. Cytoskeleton (Hoboken) 69, 235–251.

Helander HF, Fandriks L (2014). Surface area of the digestive tract—revisited. Scand J Gastroenterol 49, 681–689.

Henne WM, Kent HM, Ford MG, Hegde BG, Daumke O, Butler PJ, Mittal R, Langen R, Evans PR, McMahon HT (2007). Structure and analysis of FCHo2 F-BAR domain: a dimerizing and membrane recruitment module that effects membrane curvature. Structure 15, 839–852.

Hirokawa N, Tilney LG, Fujiwara K, Heuser JE (1982). Organization of actin, myosin, and intermediate filaments in the brush border of intestinal epithelial cells. J Cell Biol 94, 425–443.

Itoh T, Erdmann KS, Roux A, Habermann B, Werner H, De Camilli P (2005). Dynamin and the actin cytoskeleton cooperatively regulate plasma membrane invagination by BAR and F-BAR proteins. Dev Cell 9, 791–804.

Ivanov AI, Hunt D, Utech M, Nusrat A, Parkos CA (2005). Differential roles for actin polymerization and a myosin II motor in assembly of the epithelial apical junctional complex. Mol Biol Cell 16, 2636–2650.

Ivanov AI, Nusrat A, Parkos CA (2005). Endocytosis of the apical junctional complex: mechanisms and possible roles in regulation of epithelial barriers. Bioessays 27, 356–365.

Kessels MM, Dong J, Leibig W, Westermann P, Qualmann B (2006). Complexes of syndapin II with dynamin II promote vesicle formation at the trans-Golgi network. J Cell Sci 119(Pt 8), 1504–1516.

Kessels MM, Qualmann B (2002). Syndapins integrate N-WASP in receptor-mediated endocytosis. EMBO J 21, 6083–6094.

Kessels MM, Qualmann B (2004). The syndapin protein family: linking membrane trafficking with the cytoskeleton. J Cell Sci 117(Pt 15), 3077–3086.

Kessels MM, Qualmann B (2006). Syndapin oligomers interconnect the machineries for endocytic vesicle formation and actin polymerization. J Biol Chem 281, 13285–13299.

Kovacs EM, Verma S, Ali RG, Ratheesh A, Hamilton NA, Akhmanova A, Yap AS (2011). N-WASP regulates the epithelial junctional actin cytoskeleton through a non-canonical post-nucleation pathway. Nat Cell Biol 13, 934–943.

Li J, He Y, Lu Q, Zhang M (2016). Mechanistic basis of organization of the harmonin/USH1C-mediated brush border microvilli tip-link complex. Dev Cell 36, 179–189.

Li J, He Y, Weck ML, Lu Q, Tyska MJ, Zhang M (2017). Structure of Myo7b/USH1C complex suggests a general PDZ domain binding mode by MyTH4-FERM myosins. Proc Natl Acad Sci USA 114, E3776–E3785.

Loomis PA, Zheng L, Sekerkova G, Changyaleket B, Mugnaini E, Bartles JR (2003). Espin cross-links cause the elongation of microvillus-type parallel actin bundles in vivo. J Cell Biol 163, 1045–1055.

Manor U, Disanza A, Grati M, Andrade L, Lin H, Di Fiore PP, Scita G, Kachar B (2011). Regulation of stereocilia length by myosin XVa and whirlin depends on the actin-regulatory protein Eps8. Curr Biol 21, 167–172.

Millard TH, Bompard G, Heung MY, Dafforn TR, Scott DJ, Machesky LM, Futterer K (2005). Structural basis of filopodia formation induced by the IRSp53/MIM homology domain of human IRSp53. EMBO J 24, 240–250.

Mooseker MS, Graves TA, Wharton KA, Falco N, Howe CL (1980). Regulation of microvillus structure: calcium-dependent solation and cross-linking of actin filaments in the microvilli of intestinal epithelial cells. J Cell Biol 87(3 Pt 1), 809–822.

Nicholson-Fish JC, Kokotos AC, Gillingwater TH, Smillie KJ, Cousin MA (2015). VAMP4 is an essential cargo molecule for activity-dependent bulk endocytosis. Neuron 88, 973–984.

Padrick SB, Rosen MK (2010). Physical mechanisms of signal integration by WASP family proteins. Annu Rev Biochem 79, 707–735.

Peter BJ, Kent HM, Mills IG, Vallis Y, Butler PJ, Evans PR, McMahon HT (2004). BAR domains as sensors of membrane curvature: the amphiphysin BAR structure. Science 303, 495–499.

Pinette JA, Mao S, Millis BA, Krystofiak ES, Faust JJ, Tyska MJ (2019). Brush border protocadherin CDHR2 promotes the elongation and maximized packing of microvilli in vivo. Mol Biol Cell 30, 108–118.

Plomann M, Lange R, Vopper G, Cremer H, Heinlein UA, Scheff S, Baldwin SA, Leitges M, Cramer M, Paulsson M, Barthels D (1998). PACSIN, a brain protein that is upregulated upon differentiation into neuronal cells. Eur J Biochem 256, 201–211.

Postema MM, Grega-Larson NE, Neininger AC, Tyska MJ (2018). IRTKS (BAIAP2L1) elongates epithelial microvilli using EPS8-dependent and independent mechanisms. Curr Biol 28, 2876–2888 e2874.

Qualmann B, Kelly RB (2000). Syndapin isoforms participate in receptor-mediated endocytosis and actin organization. J Cell Biol 148, 1047–1062.

Qualmann B, Kessels MM, Kelly RB (2000). Molecular links between endocytosis and the actin cytoskeleton. J Cell Biol 150, F111–F116.

Qualmann B, Roos J, DiGregorio PJ, Kelly RB (1999). Syndapin I, a synaptic dynamin-binding protein that associates with the neural Wiskott–Aldrich syndrome protein. Mol Biol Cell 10, 501–513.

Ritter B, Modregger J, Paulsson M, Plomann M (1999). PACSIN 2, a novel member of the PACSIN family of cytoplasmic adapter proteins. FEBS Lett 454, 356–362.

Self T, Sobe T, Copeland NG, Jenkins NA, Avraham KB, Steel KP (1999). Role of myosin VI in the differentiation of cochlear hair cells. Dev Biol 214, 331–341.

Senju Y, Itoh Y, Takano K, Hamada S, Suetsugu S (2011). Essential role of PACSIN2/syndapin-II in caveolae membrane sculpting. J Cell Sci 124(Pt 12), 2032–2040.

Senju Y, Suetsugu S (2015). Possible regulation of caveolar endocytosis and flattening by phosphorylation of F-BAR domain protein PACSIN2/Syndapin II. Bioarchitecture 5, 70–77.

Specian RD, Neutra MR (1981). The surface topography of the colonic crypt in rabbit and monkey. Am J Anat 160, 461–472.

Steegmaier M, Klumperman J, Foletti DL, Yoo JS, Scheller RH (1999). Vesicle-associated membrane protein 4 is implicated in trans-Golgi network vesicle trafficking. Mol Biol Cell 10, 1957–1972.

Sumoy L, Pluvinet R, Andreu N, Estivill X, Escarceller M (2001). PACSIN 3 is a novel SH3 domain cytoplasmic adapter protein of the pacsin–syndapin–FAP52 gene family. Gene 262, 199–205.

Tang VW, Brieher WM (2012). alpha-Actinin-4/FSGS1 is required for Arp2/3-dependent actin assembly at the adherens junction. J Cell Biol 196, 115–130.

Tumbarello DA, Kendrick-Jones J, Buss F (2013). Myosin VI and its cargo adaptors—linking endocytosis and autophagy. J Cell Sci 126(Pt 12), 2561–2570.

van Dongen JM, Visser WJ, Daems WT, Galjaard H (1976). The relation between cell proliferation, differentiation and ultrastructural development in rat intestinal epithelium. Cell Tissue Res 174, 183–199.

Wayt J, Bretscher A (2014). Cordon Bleu serves as a platform at the basal region of microvilli, where it regulates microvillar length through its WH2 domains. Mol Biol Cell 25, 2817–2827.

Weck ML, Crawley SW, Stone CR, Tyska MJ (2016). Myosin-7b promotes distal tip localization of the intermicrovillar adhesion complex. Curr Biol 26, 2717–2728.

Yamazaki D, Oikawa T, Takenawa T (2007). Rac-WAVE-mediated actin reorganization is required for organization and maintenance of cell-cell adhesion. J Cell Sci 120(Pt 1), 86–100.

Yu IM, Planelles-Herrero VJ, Sourigues Y, Moussaoui D, Sirkia H, Kikuti C, Stroebel D, Titus MA, Houdusse A (2017). Myosin 7 and its adaptors link cadherins to actin. Nat Commun 8, 15864.

Zampini V, Ruttiger L, Johnson SL, Franz C, Furness DN, Waldhaus J, Xiong H, Hackney CM, Holley MC, Offenhauser N, *et al.* (2011). Eps8 regulates hair bundle length and functional maturation of mammalian auditory hair cells. PLoS Biol 9, e1001048.